Neutron and γ multiplicities as a function of incident neutron energy for the ^{237}Np(n, f) reaction

L. Thulliez,[1,*] O. Litaize,[2] O. Serot,[2] and A. Chebboubi[2]
[1]*IRFU, CEA, Université Paris-Saclay, 91191 Gif-sur-Yvette, France*
[2]*CEA, DEN, DER, SPRC, Cadarache, 13108 Saint-Paul-Lez-Durance, France*

(Received 11 June 2019; published 29 October 2019)

In the nuclear fission process, the excitation energy sharing mechanism between the fission fragments, the fragment angular momentum generation process and the interdependence between the two are still poorly known. The study of the neutron and γ emission characteristics as a function of fragment and compound nucleus properties brings valuable information on these mechanisms since they decrease respectively the fragment excitation energy and angular momentum. In the 1980s, Naqvi and Müller experimentally highlighted, with ^{237}Np(n, f) direct fission reactions, that only the prompt neutron multiplicity for the heavy fragment increases with the incident neutron energy. This means that the additional excitation energy goes into the heavy fragment. This data set allows one to test the different energy sharing models. This paper investigates, using the FIFRELIN fission fragment deexcitation code, the impact of the models used to assign the fragment initial state on fission observables. It focuses on the impact of a constant or an energy dependent spin cutoff model, whose parameters define the initial total angular momentum distribution, coupled with an energy sharing model based on an empirical temperature ratio law $R_T(A)$ in which fission fragments are considered to behave as a Fermi gas. It shows that both spin cutoff models succeed in reproducing the experimental neutron multiplicities which are mainly driven by the $R_T(A)$ law. However, they predict different γ observables and neutron-γ multiplicity correlations. Therefore, to infer about the validity of the two models, it is necessary to measure neutron and γ observables in correlation in order to have a deeper understanding of the fission mechanism.

DOI: 10.1103/PhysRevC.100.044616

I. INTRODUCTION

There is a growing interest in studying nuclear fission induced by fast neutrons, i.e. neutrons having an energy above hundreds of keV. For the application side, the development of GEN IV fast nuclear reactors aiming to transmute radioactive wastes, such as ^{237}Np, requires knowledge of prompt particle properties, which are of primary importance for reactor management in giving access, for example, to the fission product quantities (source of β-delayed neutrons and heat). For fundamental physics it allows one to study the fission mechanism, mainly the total excitation energy sharing mechanism between the fragments at scission, the fragment initial total angular momentum generation process, and its dependence on the compound nucleus properties and fragment initial excitation energy.

With a 2E-2V spectrometer, Naqvi and Müller [1,2] measured the average prompt neutron multiplicity as a function of the preneutron fragment mass [$\overline{\nu}(A)$], for ^{237}Np(n, f) reactions at two different incident neutron energies (E_n) equal to 0.8 MeV (energy slightly above the fission threshold) and 5.5 MeV (energy below the second-chance fission). The compound nucleus excitation energy is then perfectly known. They determined that the number of neutrons emitted by the heavy fragments increases with E_n while for the light fragments it remains constant [1,2]. This indicates that the heavy fragments take all the additional available energy. The reproduction of $\overline{\nu}(A)$ as a function of E_n is then a critical benchmark for the energy sharing models. At the moment Ruben [3], the GEF code [4] and the point-by-point model (PbP) [5] have already reproduced this behavior with different approaches (see Sec. III B).

To study the relationship between the fragment initial excitation energy and its initial total angular momentum, the neutron (n) and γ properties, such as their multiplicities (ν and M_γ), along with their correlations must be studied. To date n-γ correlation experimental studies have been mainly focused on the ^{252}Cf spontaneous fission [6–8]. In 1972, Nifenecker [6] showed, based on $\overline{M}_\gamma(A)$ from John [9] and $\overline{\nu}(A)$ from Bowman [10], that on average there is a positive correlation between $\overline{M}_\gamma$ and $\overline{\nu}$ (for a single fragment). However, as already mentioned by Talou [11], considering the way John built $\overline{M}_\gamma(A)$, Nifenecker's result cannot be considered. In 1989, Glässel [12] determined that on average a weak correlation exists: $\overline{M}_\gamma \propto 0.16\overline{\nu}$ (for both fragments) and, on an event-by-event basis, $\nu \propto -0.02 M_\gamma$ (for both fragments). This highlights the n-γ competition and the increase of the fragment angular momentum with energy. This result was confirmed by Marcath in 2018 [8] who found $\nu \propto -0.0016(\pm 0.0096)\, M_\gamma$. In 1989, Fréhaut [13] found that the average γ energy ($\langle \epsilon_\gamma \rangle$) increases and that $\overline{M}_\gamma$ remains constant when E_n increases, for different fissioning systems such as ^{238}Np. Therefore on average the total angular momentum is independent of the total excitation energy. In 2016, Wang [7] found that $\overline{M}_\gamma(\nu)$ is linear with a slightly positive slope for the light fragments

*loic.thulliez@cea.fr

($85 < A < 123$), is linear with a large positive slope in the symmetry region ($124 < A < 131$), and has a complex shape for heavy fragments ($132 < A < 167$).

To summarize, at the moment different energy sharing models, with contradictory approaches, reproduce well the experimental $\overline{\nu}(A)$. To infer about the validity of the different models, their predictions have to be compared with experimental n-γ correlations. In this paper we offer to shed new light on the energy sharing and total angular momentum generation processes with the fission fragment deexcitation code FIFRELIN developed at CEA-Cadarache (France) [14–16]. This code has two descriptions of the initial total angular momentum distribution, one being independent of the fragment initial excitation energy and one being dependent on it [17,18]. As a consequence the impact of a weak or a strong relationship between the initial excitation energy and the initial total angular momentum can be investigated in comparing the different prompt particle observable predictions associated with each distribution.

Section II briefly discusses the main features of the code. Special attention is paid to the fragment initial state assignment (energy sharing mechanism and initial total angular momentum distribution). Section III first describes the input data used to study ^{237}Np(n, f) fast fission reactions. Then it presents the observables predicted with the two initial total angular momentum distributions for ^{237}Np(n, f) reactions at $E_n = 0.8$ MeV and $E_n = 5.5$ MeV. The predictions are compared with the available data, mostly depending on the fragment masses (for a given mass, the observables are averaged over the initial states). The predicted neutron observables are discussed before presenting the γ ones. Then the initial total angular momentum dependence on the compound nucleus properties and initial fragment excitation energy are investigated in studying fission observables as a function of the total kinetic energy and ν-M_γ correlation matrices built on an event-by-event basis (for a given initial state the observables are averaged over the fragment masses).

II. MODELIZATION OF THE FISSION FRAGMENT DEEXCITATION WITH FIFRELIN

A. A brief overview of the code

The FIFRELIN code is a deexcitation code dealing with binary fission (ternary particle emission is neglected). It starts from fully accelerated fragments having recovered their ground state deformation during the Coulomb repulsion step. The simulation starts from highly excited neutron rich nuclei. The deexcitation of the two fragments begins by defining a specific fragmentation, i.e., the mass and nuclear charge of each of them. The mass of one fragment is sampled in an experimental preneutron fragment mass yield $[Y(A)]$ and then the nuclear charge is sampled using the empirical model proposed by Wahl [19,20], which account for the charge polarization and the odd-even effects. The complementary fragment mass and charge are deduced from the conservation laws. The fragment kinetic energies are sampled from a Gaussian law defined by an average total kinetic energy $\langle \mathrm{TKE} \rangle (A)$ and a standard deviation $\sigma_{\mathrm{TKE}}(A)$ coming from experimental distributions $[Y(\mathrm{TKE}|A)]$. The kinetic energy KE of each fragment is deduced from the linear momentum conservation law. With those pieces of information and an energy balance calculation the total excitation energy (TXE) to be shared between the two fragments is computed. The models used to share TXE and to assign an initial state to both nuclei, i.e., an excitation energy E, a total angular momentum J, and a parity π, will be detailed in Sec. II B. Starting from an initial state, the code performs the fragment deexcitation in going from this initial state to a final state in emitting a prompt particle (a neutron, a γ, or an electron). This is performed within a Monte Carlo Hauser-Feschbach framework, based on Bečář's algorithm [21], and extended to the n-γ emission by Regnier [16]. This algorithm allows one to follow the evolution of the fragment state (E, J, π) during the deexcitation cascade and to take into account both statistical and nuclear structure uncertainties associated with fission observables.

In this paper, the main ingredients to calculate the transition probabilities are the *composite Gilbert- Cameron* nuclear level densities [22] using an energy dependent level density parameter [23], the *Köning-Delaroche* neutron transmission coefficients [24], and the *enhanced generalized Lorentzian* photon strength functions [25] for electric dipole radiations. Other multipolarities are accounted for as discussed in Ref. [23]. At low energy, the FIFRELIN code uses all the experimental level schemes and γ-ray and electron (the internal conversion coefficient are from the BRICC evaluation [26]) transition probabilities available in the RIPL-3 database [23]. A detailed description of the code can be found in Refs. [14,15].

B. Fission fragment initial state assignment

Once the fragmentation is known (A, Z, KE), the initial state of each primary fragment has to be defined. This procedure starts with an energy balance calculation to determine the total excitation energy:

$$\mathrm{TXE} = B^{FF_H} + B^{FF_L} - B^{\mathrm{CN}} + S_n^{\mathrm{CN}} + E_n - \mathrm{TKE} \quad (1)$$

with TXE the total excitation energy, B^{FF_H}, B^{FF_L}, and B^{CN} the fission fragments (H and L stand respectively for heavy and light) and compound nucleus (CN) binding energies, S_n^{CN} the compound nucleus neutron separation energy, E_n the incident neutron kinetic energy, and TKE the sum of the two complementary fragment kinetic energies.

To share TXE between the two fragments it is assumed that each fragment excitation energy (E) is made, after the full acceleration, of an intrinsic part (E^{int}) and a collective part (E^{coll}):

$$E = E^{\mathrm{int}} + E^{\mathrm{coll}}. \quad (2)$$

The collective part is assumed to essentially come from the rotation of the fragment ($E^{\mathrm{coll}} = E^{\mathrm{rot}}$) and is simply described by considering a rotating liquid drop:

$$E^{\mathrm{rot}} = \frac{J(J+1)\hbar^2}{2I_{\mathrm{rig}}}, \quad (3)$$

where I_{rig} is the spheroid rigid moment of inertia and J the initial total angular momentum. This latter value is computed

by using the spin distribution following Bethe's work [27]:

$$P(J|\sigma^2) = \frac{2J+1}{2\sigma^2}\exp\left(-\frac{(J+1/2)^2}{2\sigma^2}\right) \quad (4)$$

with σ^2 the spin cutoff parameter shaping the distribution.

In FIFRELIN, two spin cutoff models are available [17,18]. With the first one, called *constant* ($\sigma = K$), the light and the heavy fragment total angular momenta are sampled from Eq. (4), having each a free constant spin cutoff parameter,

$$\sigma_L = K_L \quad \text{and} \quad \sigma_H = K_H. \quad (5)$$

With the second one, named *energy dependent* [$\sigma(E)$], the light and heavy fragment angular momenta are sampled in Eq. (4) with a spin cutoff parameter depending on the fragment properties and excitation energy [17,18,23]:

$$\sigma(E) = f_\sigma\sqrt{\frac{a}{\tilde{a}}}\sqrt{I_{\text{rig}}T}, \quad (6)$$

$$a(E) = \tilde{a}\left(1 + \delta W\frac{1-e^{-\gamma U}}{U}\right), \quad (7)$$

$$\tilde{a} = \alpha A + \beta A^{\frac{2}{3}}, \quad (8)$$

$$U = E - \Delta \quad (9)$$

with f_σ a free parameter introduced to renormalize the initial total angular momentum value. This is needed to reproduce the target observable as explained in Sec. III A. $a(E)$ and $\tilde{a}$ are respectively the Ignatyuk level density parameter and its asymptotic value (level density parameter when all the shell corrections are damped) [28]. In $a(E)$, δW represents the shell corrections and γ the shell correction damping parameter varying as $A^{-1/3}$. In $\tilde{a}$ the α and β parameters are respectively the volume and surface contributions to the level density parameter [23]. $T = \sqrt{\frac{U}{a}}$ is the nuclear temperature, where U is defined as the excitation energy taking into account the pairing energy Δ.

The *constant* spin cutoff parameter is introduced because of our limited understanding of the fragment initial total angular momentum generation process while the *energy dependent* one is based on statistical considerations. In 1936, Bethe [27], in considering the nucleus as a Fermi gas, defined the nucleus total angular momentum dispersion in counting the contribution of each nucleon above the Fermi energy to the dispersion of the projection of the total angular momentum on the z axis (M^2). When the nucleus energy increases, more and more nucleons populate energy levels above the Fermi energy and consequently the spin cutoff parameter (the dispersion) increases as $\sigma = \sqrt{I_{\text{rig}}T}$. However, microscopic level densities studies have shown that σ^2/T is not a constant [23], which led to the inclusion of additional shell effects ($\sqrt{a/\tilde{a}}$) to Bethe's formulation, as suggested by various authors [23,29,30].

Once the rotational energy of the primary fission fragments is known, the total intrinsic excitation energy TXE$^{\text{int}}$ [Eq. (10)] can be shared between the two complementary fragments considered as a Fermi gas, whose intrinsic energy is given by Eq. (11):

$$\text{TXE}^{\text{int}} = \text{TXE} - \left(E_L^{\text{rot}} + E_H^{\text{rot}}\right) = E_L^{\text{int}} + E_H^{\text{int}}, \quad (10)$$

$$E^{\text{int}} = aT^2, \quad (11)$$

Equation (10) shows that an anticorrelation exists between E_L^{int} and E_H^{int} (via TXE$^{\text{int}}$).

Since the fragment temperature T is not known and microscopic models do not sufficiently accurately predict the energy sharing between the fragments, an empirical temperature ratio law $R_T(A)$ has been introduced in FIFRELIN [14]. It describes the evolution of the ratio of the light fragment temperature over the heavy fragment one ($R_T = T_L/T_H$) as a function of the preneutron fragment mass. At symmetry ($A_H = A_L = A_{\text{CN}}/2$) the temperature ratio is set equal to $R_T^{\text{sym}} = 1$ because the two fragments are identical. This law is ruled by two free parameters, R_T^{78} and R_T^{132}, respectively associated to the doubly magic nuclei $A_L = 78$ (with $N = 50$ and $Z = 28$) and $A_H = 132$ (with $N = 82$ and $Z = 50$). It encapsulates the fact that a doubly magic nucleus has a low deformation energy that will be converted in intrinsic energy after the relaxation phase during which the nucleus recover its ground state deformation. Because this kind of nucleus has a low deformation energy, it will have a low intrinsic excitation energy then a low temperature. For low compound nucleus excitation energy, T_H ($A_H = 132$) and T_L ($A_L = 78$) will be low and then R_T^{132} and R_T^{78} will be high and low respectively ($R_T = T_L/T_H$). To set the R_T values for a given fragmentation, a linear interpolation is performed between R_T^{sym}, R_T^{132}, and R_T^{78}. An $R_T(A)$ law is chosen for a given compound nucleus with a specific excitation energy.

Given TXE$^{\text{int}}$, the light and heavy fragment intrinsic excitation energies are computed using the following relations, obtained in substituting Eq. (11) in Eq. (10):

$$E_L^{\text{int}} = \frac{\text{TXE}^{\text{int}}}{1+\frac{a_H}{a_L R_T^2}} \quad \text{and} \quad E_H^{\text{int}} = \frac{\text{TXE}^{\text{int}}}{1+\frac{a_L R_T^2}{a_H}}. \quad (12)$$

To solve this system of two implicit equations ($a_{L,H}$ depends on $E_{L,H}$), the rotational parts need to be subtracted from TXE using the knowledge of J [Eqs. (3) and (10)]. This latter quantity depends on the spin cutoff parameter σ^2. With the *constant* spin cutoff model [Eq. (5)], this system is solved by sampling once for all J_L and J_H and then performing the iterative process. With the *energy dependent* model [Eq. (6)], $\sigma^2(E)$ changes at each iteration, and so does J. Solving this system can then be unstable. To overcome this difficulty the average value of the $P(J|\sigma^2(E))$ distribution given by Eq. (13) is assigned to the fragment inside the iterative routine. This will not change in average the fission observable values and allows one to keep an energy dependent spin cutoff parameter:

$$J = \bar{J} = \sqrt{\frac{\pi}{2}}\sigma(E^{\text{int}}) - \frac{1}{2}. \quad (13)$$

To conclude, two spin cutoff models and an energy dependent $R_T(A)$ law [$R_T(A) = T(A_L)/T(A_H)$] are available to study the energy sharing mechanism and its relationship with the total angular momentum generation process. With the *constant* spin cutoff model, there are four free parameters (R_T^{78}, R_T^{132}, K_L, and K_H), whereas with the *energy dependent* model only three parameters have been introduced (R_T^{78}, R_T^{132}, and f_σ). These parameters are set to reproduce target observables which are chosen here to be the average total prompt neutron

multiplicity ($\overline{\nu}$) as well as $\overline{\nu}_L$ and $\overline{\nu}_H$. All the other prompt particle properties are then code predictions.

After a quick presentation of the code input data, the impact of the $R_T(A)$ law and the spin cutoff models on the fission observables are studied on the ^{237}Np(n, f) reaction at $E_n = 0.8$ MeV and $E_n = 5.5$ MeV.

III. ^{237}Np(n, f) FAST FISSION REACTIONS

A. Input data and target observables

The ^{237}Np(n, f) preneutron fragment mass yields are extracted from the EXFOR database, which is filled with data published in a report by Müller and Naqvi [1] in 1981 and not from [2] published in 1986. These data are provided with a 0.5 mass step because the data analysis was performed with this step despite a 2.1 spectrometer mass resolution [1]. Therefore, to have an integer mass, we performed an average between two adjacent half-masses. The results are presented in Fig. 1. The total kinetic energy associated with the fragmentation is determined with the help of the experimental data $\langle \mathrm{TKE} \rangle(A)$ and $\sigma_{\mathrm{TKE}}(A)$ (Figs. 2 and 3) which are also extracted from the EXFOR database. Here the same averaging procedure as for the mass yields has been applied. At $E_n = 0.8$ MeV, for $119 \leqslant A \leqslant 122$, $\sigma_{\mathrm{TKE}}(A)$ is equal to 0 MeV (the data might not have been provided to EXFOR) [31] and for $A = 124$ it is approximately equal to 13 MeV, which is higher by 4–5 MeV than for its neighbor mass ones. Consequently the masses associated to these σ_{TKE} are not considered anymore in the following. The results presented in Fig. 2 show that, at $E_n = 5.5$ MeV, $\langle \mathrm{TKE} \rangle(A)$ is always lower than the one at $E_n = 0.8$ MeV whatever the fragment mass is, because when E_n increases fragments have more deformed shapes leading to a weaker Coulomb interaction. According to Eq. (1), when E_n increases, the extra total excitation energy (ΔTXE) to be shared between the fragments is given by the total kinetic energy variation (ΔTKE) in addition to the extra incident neutron energy (ΔE_n). Here, when E_n increases from 0.8 to 5.5 MeV, the average TKE decreases from 174.9 to 172.4 MeV ($\Delta\mathrm{TKE} = -2.5$ MeV) which contributes approximately a third of the total excitation energy variation, equal to $\Delta\mathrm{TXE} = 7.3$ MeV (on average, the reaction Q value increases by 0.1 MeV).

The model parameters are set to reproduce target observables, which are here $\overline{\nu}$, $\overline{\nu}_L$, and $\overline{\nu}_H$. $\overline{\nu}$ depends mainly on $\overline{\mathrm{TXE}}$ given by the $Y(A)$ and TKE(A) experimental inputs [see Eq. (1) as well as Figs. 1 and 2]. In addition $\overline{\nu}_L$ and $\overline{\nu}_H$ strongly rely on the $R_T(A)$ law, taking into account the impact of the fragment deformation energy at scission in the fragment excitation energy after the Coulomb repulsion step (see Sec. II). The choice of the spin distribution model [Eq. (4) and Eqs. (5) or (6)] also impact the neutron observables in two ways: first because the intrinsic excitation energy is computed in subtracting the rotational energy of the two fragments, and second because of the n-γ competition process. In fact if a neutron emission is energetically possible but the total angular momentum is too high, such as when the daughter nucleus has no available state, the transition is forbidden. Only γ emission is then possible. The impact of the spin cutoff model choice on

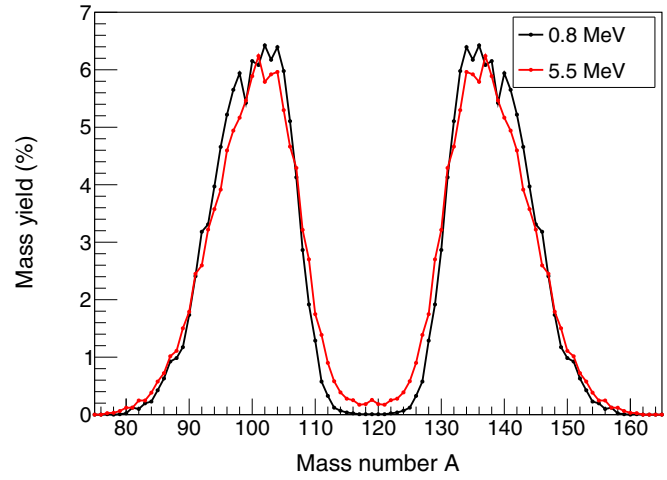

FIG. 1. Preneutron fragment mass yields, for ^{237}Np(n, f) reactions at 0.8 and 5.5 MeV neutron energies [1,2,31].

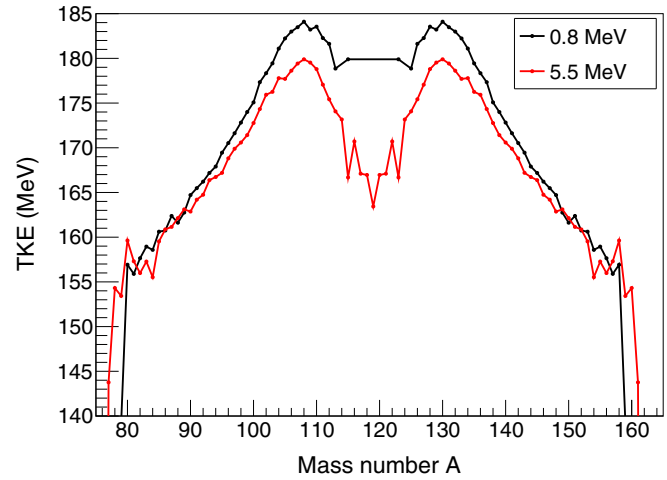

FIG. 2. Average total kinetic energy as a function of the preneutron fragment mass, for ^{237}Np(n, f) reactions at 0.8 and 5.5 MeV neutron energies [1,2,31].

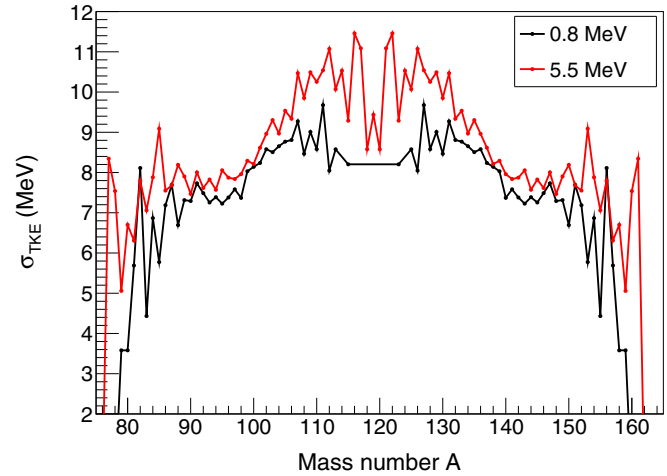

FIG. 3. Standard deviation of the total kinetic energy distribution as a function of the preneutron fragment mass, for ^{237}Np(n, f) reactions at 0.8 and 5.5 MeV neutron energies [1,2,31].

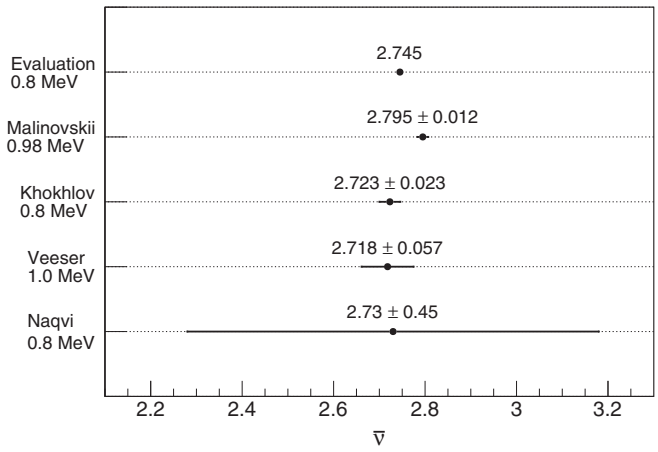

(a) $E_n = 0.8$ *MeV*.

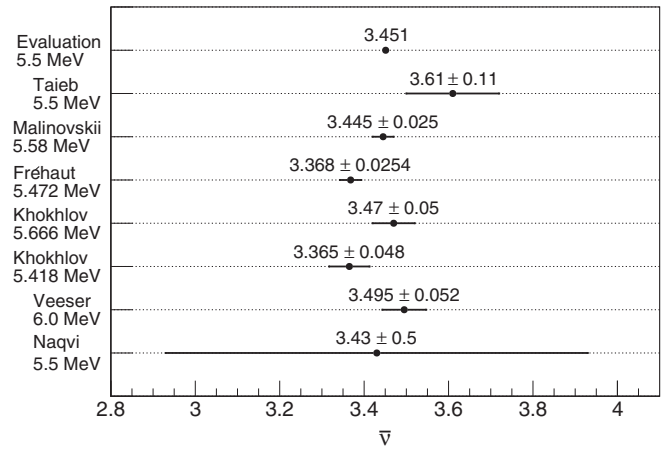

(b) $E_n = 5.5$ *MeV*.

FIG. 4. Average total prompt neutron multiplicities, with their statistical uncertainties, for ^{237}Np(n, f) reactions at 0.8 and 5.5 MeV neutron energies. Experimental data are extracted from EXFOR [31], and come from Naqvi [2], Veeser [32], Khokhlov [33], Malinovskii [34], Taieb [35] and the evaluated data from JEFF-3.3 [36].

fission observables has already been investigated on ^{252}Cf(sf) in Refs. [17,18]. These studies have shown that it is small for neutrons but is important for γ observables. Studying the impact of the spin cutoff model for other fissioning systems and different excitation energies could guide future studies.

The available experimental $\overline{\nu}$ associated with ^{237}Np(n, f) are summarized in Fig. 4. At $E_n = 0.8$ MeV [Fig. 4(a)] the data lead us to set the target observable equal to 2.73. The associated uncertainty is 0.45, which is dominated by Naqvi's uncertainty. $\overline{\nu}_L$ and $\overline{\nu}_H$ are taken from Naqvi [2] and are respectively equal to 1.59 and 1.14. At $E_n = 5.5$ MeV [Fig. 4(b)], the evaluation of the target observable is more difficult since experimental $\overline{\nu}$ varies from 3.368 (Fréhaut [37]) to 3.61 (Taieb [35]), which do not overlap even inside their uncertainties. The JEFF-3.3 evaluated value, equal to 3.451, is defined as the target observable since the evaluation process takes into account the experimental points. The associated uncertainty is 0.52, which is also dominated by Naqvi's one. $\overline{\nu}_L$ and $\overline{\nu}_H$ are respectively equal to 1.59 ± 0.08 and 1.87 ± 0.08 [2].

B. Prompt neutron observables

To date, Ruben [3], the GEF code [4], and the point-by-point model (PbP) [5] have already succeeded in reproducing the result that only the heavy fragment neutron multiplicity increases when E_n increases. To do so, Ruben considers a scission point model where the additional neutron energy goes into fragment intrinsic excitation energies which change the temperature-dependent shell corrections. This impacts the fragment deformation and E^{int}. The heavy fragment high negative shell corrections start to be damped because E^{int} increases. This allows one to reproduce the neutron emission variation for heavy fragments when E_n increases. The GEF code uses the energy sorting mechanism [38] in which the fission fragment properties are described with the *constant temperature* nuclear level density model [22,23]. In this approach, at scission, the two touching fragments behave like two thermodynamic objects, having a constant temperature given by Von Egidy's parametrization [39] in which T depends only on the fragment mass and shell corrections. In most cases T_L is higher than T_H, leading to an energy transfer from the light to the heavy fragment. This explains why the heavy fragments emit more neutrons as the compound nucleus energy increases. On the other hand, the PbP model [5] describes the two fragments at scission as a system in statistical equilibrium, in which the fragment properties are described with the Fermi gas nuclear level density model and Ignatyuk's superfluid model level-density parameter. Because the level density parameter for heavy nuclei increases with excitation energy (while it remains constant for other nuclei) the increase of $\overline{\nu}(A)$ for heavy fragments can be reproduced. With these ingredients the total excitation energy is shared, using an algorithm similar to the one presented in Sec. II B. The FIFRELIN neutron observables predicted with the two spin cutoff models are now presented.

The values of the parameters used to reproduce $\overline{\nu}$ are listed in Table I and the associated average neutron multiplicities are presented in Table II. With both the *constant* and *energy dependent* spin cutoff models the predicted $\overline{\nu}$ are similar to the target observables, being equal to 2.73 and to 3.45 respectively at $E_n = 0.8$ MeV and $E_n = 5.5$ MeV. $\overline{\nu}_L$ and $\overline{\nu}_H$ absolute values and variations are also similar to the experimental data ones: when E_n increases $\overline{\nu}_L$ remains constant while $\overline{\nu}_H$ increases.

TABLE I. Model parameters allowing to reproduce the average total prompt neutron multiplicities for ^{237}Np(n, f) reactions at 0.8 and 5.5 MeV neutron energies.

E_n (MeV)	Model	R_T^{78}	R_T^{132}	σ_L ($\hbar$)	σ_H ($\hbar$)	f_σ
0.8	$\sigma = K$	0.9	1.05	10.0	7.0	
	$\sigma(E)$	0.9	1.05			1.25
5.5	$\sigma = K$	0.95	0.75	10.0	10.5	
	$\sigma(E)$	0.95	0.75			1.50

TABLE II. Average total prompt neutron multiplicities for ^{237}Np(n, f) reactions at 0.8 and 5.5 MeV neutron energies. The simulation statistical uncertainty is $\sigma_\nu \approx 1 \times 10^{-3}$.

E_n (MeV)	Data	$\overline{\nu}_L$	$\overline{\nu}_H$	$\overline{\nu}$
0.8	Target			2.73 ± 0.45
	Naqvi	1.59	1.14	2.73 ± 0.45
	$\sigma = K$	1.603	1.148	2.752
	$\sigma(E)$	1.599	1.194	2.794
5.5	Target			3.45 ± 0.52
	Naqvi	1.59 ± 0.08	1.87 ± 0.08	3.43 ± 0.50
	$\sigma = K$	1.607	1.914	3.521
	$\sigma(E)$	1.571	1.929	3.501

The predicted neutron multiplicity as a function of mass $[\overline{\nu}(A)]$ presented in Fig. 5 points out that both models predict a constant $\overline{\nu}(A)$ as a function of E_n for the light fragments, which agrees well with the experimental data. Only the heavy fragment neutron multiplicity varies between +0.5 and +1.0 neutron when E_n increases, which is also consistent with the data within their uncertainties. The comparison between Figs. 5 and 6 shows that the $\overline{\nu}(A)$ variation as a function of E_n is correlated to an initial total angular momentum variation $[\Delta\overline{J}_A(E_n)]$: the heavy fragment angular momentum increases roughly by 4.4 $\hbar$ with both spin cut-off models, whereas for the light fragments $\Delta\overline{J}_L = 0\,\hbar$ with the *constant* model (as expected since σ_L does not vary) and $\Delta\overline{J}_L = 2.1\,\hbar$ with the *energy dependent* model. Although $\overline{J}_L$ varies with this later model contrary to the *constant* model one, the neutron emission is not changed because this spin variation is coupled to an energy variation $\Delta\overline{E}_L = 0.4$ MeV, which at the end does not impact the n-γ competition.

These accurate neutron observable predictions mean that the $R_T(A)$ empirical law $[R_T(A) = T_L/T_H = T(A_L)/T(A_H)]$ coupled with both spin cutoff models (along with the model parameters presented in Table I) are suited to describe the

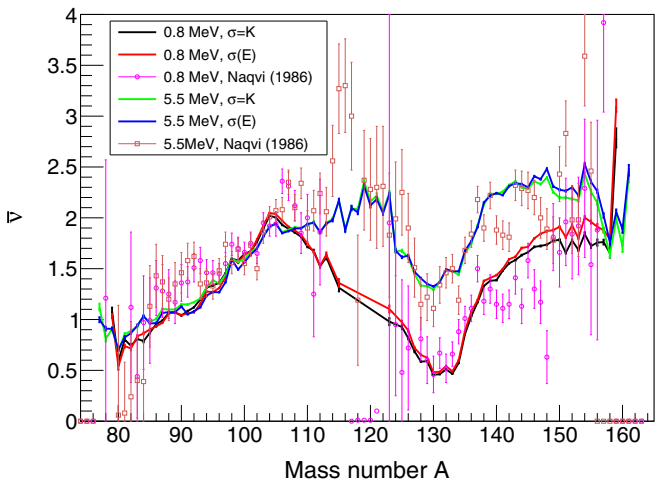

FIG. 5. Average prompt neutron multiplicity as a function of the preneutron fragment mass for ^{237}Np(n, f) reactions at 0.8 and 5.5 MeV neutron energies.

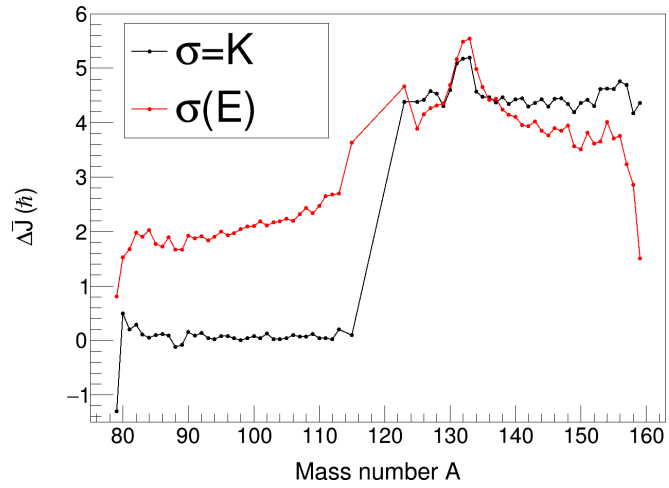

FIG. 6. Difference between the average initial total angular momenta at 0.8 and 5.5 MeV neutron energies, as a function of the preneutron fragment mass for ^{237}Np(n, f) reactions, for two spin cutoff models.

energy sharing mechanism between the two fragments. This validates the initial state assignment procedure of FIFRELIN for the fast fission energy range, which has been already validated for spontaneous and thermal fission [15]. In going from $E_n = 0.8$ MeV to $E_n = 5.5$ MeV, the target observables are well reproduced in changing insignificantly R_T^{78} (from 0.90 to 0.95), in decreasing R_T^{132} (from 1.05 to 0.75), and in tuning either σ_H (*constant* model) or f_σ (*energy dependent* model) such that $\overline{J}_H$ increases by 4.5 $\hbar$. The excitation energy sharing mechanism is therefore mainly dependent on the $R_T(A)$ law evolution as a function of E_n and not on the spin cutoff model as long as the average total angular momentum of the heavy fragments increases with E_n.

In this study, temperature ratios R_T^{78} and R_T^{132} are fitted to reproduce $\overline{\nu}$ as well as $\overline{\nu}_L$ and $\overline{\nu}_H$. An increase of the ratio $R_T = T_L/T_H$ could come from a higher increase of T_L compared to T_H or a higher decrease of T_H compared to T_L (the reciprocal assessment is true). Here, the net effect of the R_T^{78} and R_T^{132} variations on the fragment temperature (average of the Fermi gas temperature over all the fragment having a given mass) are shown in Fig. 7. As can be seen, for both spin cutoff models the temperatures as a function of both A and E_n are similar. It also shows that when E_n increases T_L remains almost constant (for $A < 95$ the temperature increase is less than 0.15 MeV) whereas T_H increases between 0.2 and 0.6 MeV. As a result, on average T_H is higher than T_L. Since T_H increases more than T_L, mechanically E_H increases more than E_L. Therefore the shell effects present at low energy in $a(E)$ [Eq. (7)] for the heavy spherical nucleus are partially damped. The level density parameter $a(E)$ starts to converge toward its asymptotic value $\tilde{a}$. Since $\tilde{a}$ depends exclusively on the nucleus mass [Eq. (8)], $a_H(E)$ is almost systematically greater than $a_L(E)$.

Recalling that $a(E)$ can be seen as the nucleus heat capacity in a thermodynamic view, it is then obvious that the heavy fragment has a higher energy than its light partner and therefore emits more neutrons. In using the iterative process

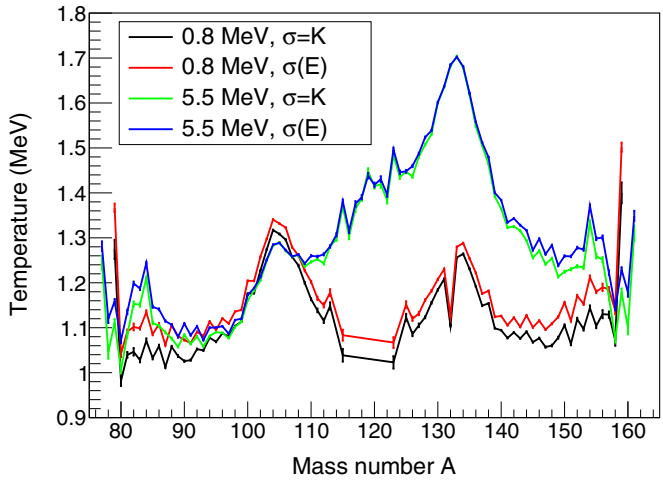

FIG. 7. Fragment temperature as a function of the preneutron fragment mass for ^{237}Np(n, f) reactions at 0.8 and 5.5 MeV neutron energies, for two spin cutoff models.

presented in Sec. II, the additional total excitation energy goes mechanically into the heavy fragment. Here, the assumption of a slow (with respect to the neutron characteristic time) scission process is made. A thermal equilibrium is reached. No energy fluctuations are taken into account that could appear in a fast scission process. As a consequence these results give confidence in a slow scission dynamic. The outputs of this process, the initial state distributions, are presented in Figs. 8 and 9 respectively for the *constant* model and the *energy dependent* model. For both models the light fragment initial state distributions remain approximately the same while the heavy fragment ones spread out with E_n. The narrow initial state distributions obtained with the *energy dependent* model (Fig. 9) are the consequence of the energy sharing process in which the initial total angular momentum is defined by Eq. (13). The shape of this distribution is driven by the spin cutoff parameter which is a root square function of the excitation energy [Eq. (6)]. These distributions show that $R_T(A)$ variations lead to increase $\overline{E}_H$ roughly by 7.2 MeV while $\overline{E}_L$ remains approximately constant (with the *energy dependent* model, it slightly increases by 0.4 MeV). Recalling that when E_n increases the additional TXE to share between the two fragments is 7.3 MeV, the simulations confirm that the evolution of $\overline{\nu}(A)$ as a function of E_n is because the heavy fragments take roughly all the additional excitation energy.

To conclude, at a given E_n, a simulation performed with a unique $R_T(A)$ law coupled with both spin cutoff models accurately predicts the neutron observables. This means that the neutron observables are not suited for inferring about the spin cutoff model's validity. However, since $\overline{J}_L$ remains constant with the *constant* model and increases by 2.1 $\hbar$ with the *energy dependent* one, the two models should predict different γ observables which can be used to infer about a weak or a strong relationship between the fragment initial excitation energy and total angular momentum.

TABLE III. Prompt fission γ observables for ^{237}Np(n, f) reactions at 0.8 and 5.5 MeV neutron energies with a coincidence time window $\Delta t = 3$ ns and without energy detection threshold. The simulation uncertainties are $\sigma(\langle E_\gamma^{\rm tot}\rangle) \approx 4 \times 10^{-3}$ MeV, $\sigma(\langle \epsilon_\gamma\rangle) \approx 5 \times 10^{-4}$ MeV, $\sigma(\overline{M}_\gamma) \approx 6 \times 10^{-3}$, $\sigma(\overline{M}_{\gamma,L,H}) \approx 5 \times 10^{-3}$.

E_n (MeV)	Data	$\langle E_\gamma^{\rm tot}\rangle$ (MeV)	$\langle \epsilon_\gamma\rangle$ (MeV)	$\overline{M}_\gamma$	$\overline{M}_{\gamma,L}$	$\overline{M}_{\gamma,H}$
0.8	Fréhaut	6.77	0.928	7.35		
	$\sigma = K$	7.54	0.888	8.48	5.72	2.76
	$\sigma(E)$	7.19	0.883	8.14	4.71	3.44
5.5	Fréhaut	7.37	1.00	7.42		
	$\sigma = K$	8.82	0.872	10.11	5.74	4.39
	$\sigma(E)$	8.94	0.845	10.58	5.69	4.90

C. Prompt γ observables

γ emission is the main deexcitation channel decreasing the nucleus angular momentum, and therefore γ observables contain the necessary information to infer about each spin cutoff model's validity. The code predictions are now presented, compared with the scarce experimental data, and discussed. In the following the simulations are performed with a coincidence time window $\Delta t = 3$ ns and without detection energy threshold ($\epsilon_\gamma^{\rm thr} = 0$ MeV).

Only Fréhaut [13] has experimentally studied n-γ correlations for the fast fission reactions. For ^{237}Np(n, f) reactions, he found that the average total γ energy ($\langle E_\gamma^{\rm tot}\rangle$) and the average γ energy ($\langle \epsilon_\gamma\rangle$) as a function of $\overline{\nu}$ have a positive linear trend, while $\overline{M}_\gamma(\overline{\nu})$ is almost a constant. Table III presents the code predictions along with Fréhaut's results (the data are obtained with the help of the linear equations given in [13] and with Fréhaut's total neutron multiplicities presented in Fig. 4). It shows that both spin cutoff models overestimate $\langle E_\gamma^{\rm tot}\rangle$ roughly by 0.6 and 1.5 MeV, and $\overline{M}_\gamma$ by one γ and three γ's respectively at $E_n = 0.8$ MeV and $E_n = 5.5$ MeV. Such discrepancies are not surprising because Fréhaut's $\overline{\nu}$ underestimate by at least 0.2 neutron the accepted values (Sec. III A). Overall average total γ observables will not help one to infer about the model validity. However, because $\overline{M}_\gamma(A)$ (Fig. 10) is the observable counterpart of $\overline{J}(A)$ (Fig. 6), for the light fragments, when E_n increases $\overline{M}_\gamma(A)$ remains the same ($\Delta\overline{M}_{\gamma,L} = 0.02$, $\Delta\overline{J}_L = 0\,\hbar$) with the *constant* model and $\overline{M}_\gamma(A)$ increases ($\Delta\overline{M}_{\gamma,L} = 0.98$, $\Delta\overline{J}_L = 2.1\,\hbar$) with the *energy dependent* model. Considering the different model predictions, new experiments determining $\overline{M}_\gamma(A)$ as a function of E_n will be a critical test for the models.

D. Correlations between prompt particle observables

The fragment initial total angular momentum comes from collective excitation modes (mainly the bending and wriggling modes) [40], the Coulomb torque exerted by one fragment on the other during the acceleration phase after the scission (the more deformed the fragments are, the stronger the Coulomb torque is) [41–43], and the orbital angular momentum of the incident neutron (when E_n increases the incident neutron has a higher orbital angular momentum). The

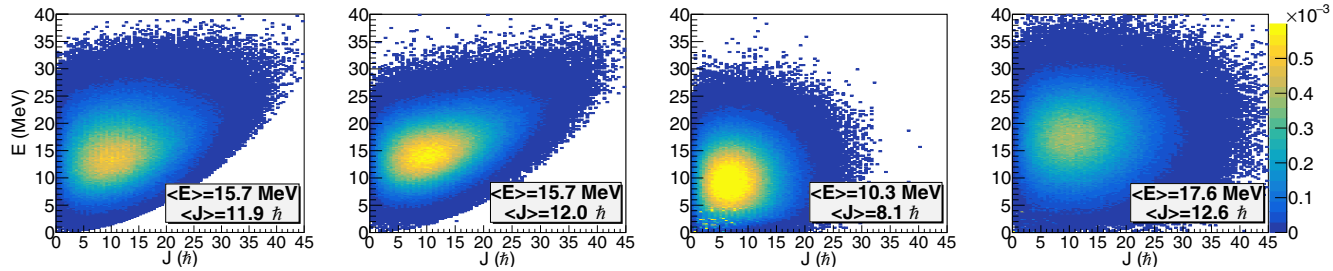

(a) *Light FF,* $E_n = 0.8$ *MeV.* (b) *Light FF,* $E_n = 5.5$ *MeV.* (c) *Heavy FF,* $E_n = 0.8$ *MeV.* (d) *Heavy FF,* $E_n = 5.5$ *MeV.*

FIG. 8. Constant spin cutoff model: Initial state (E, J) distributions for the two fission fragment (FF) mass groups for ^{237}Np(n, f) reactions at 0.8 and 5.5 MeV neutron energies (for 10^6 fissions). The E and J binnings are respectively 200 keV and 0.5 $\hbar$. The distributions have been normalized by the count numbers.

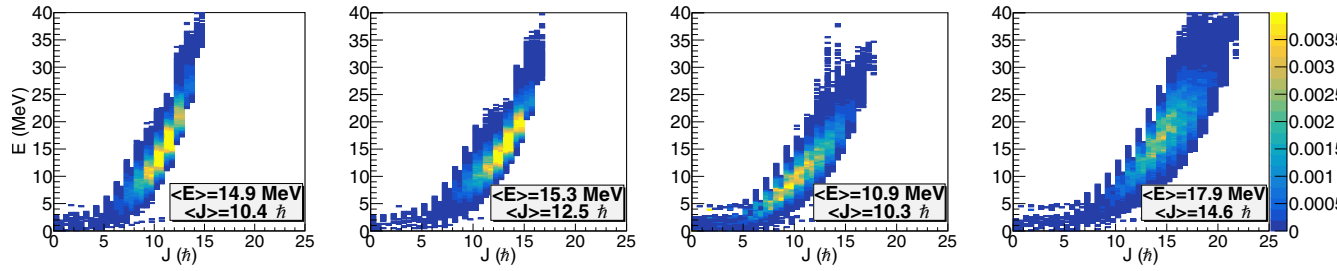

(a) *Light FF,* $E_n = 0.8$ *MeV.* (b) *Light FF,* $E_n = 5.5$ *MeV.* (c) *Heavy FF,* $E_n = 0.8$ *MeV.* (d) *Heavy FF,* $E_n = 5.5$ *MeV.*

FIG. 9. Energy dependent spin cutoff model: Initial state (E, J) distributions for the two fission fragment (FF) mass groups for ^{237}Np(n, f) reactions at 0.8 and 5.5 MeV neutron energies (for 10^6 fissions). The E and J binnings are respectively 200 keV and 0.5 $\hbar$. The distributions have been normalized by the count numbers.

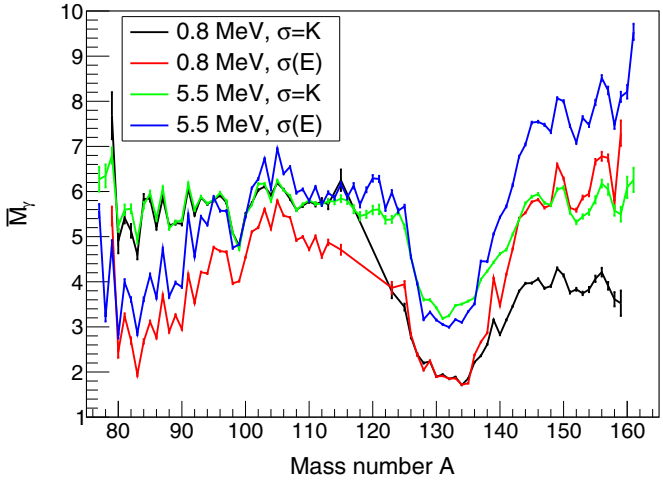

FIG. 10. Average prompt fission γ multiplicity as a function of the preneutron fragment mass for ^{237}Np(n, f) reactions at 0.8 and 5.5 MeV neutron energies with a coincidence time window $\Delta t =$ 3 ns and without detection energy threshold, for two spin cutoff models.

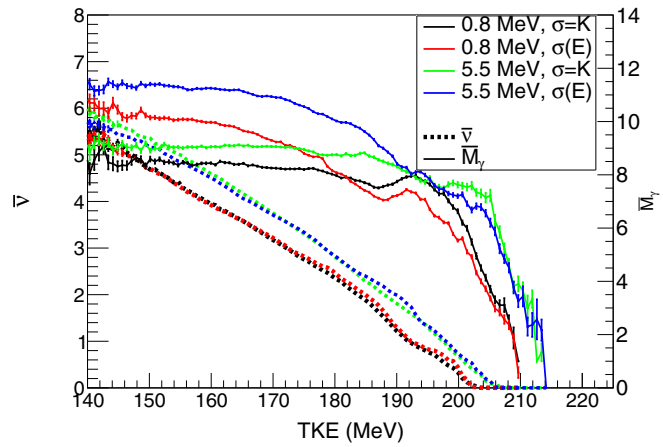

FIG. 11. Average total prompt neutron multiplicity (left scale) and γ multiplicity (right scale) as a function of the total kinetic energy for ^{237}Np(n, f) reactions at 0.8 and 5.5 MeV neutron energies, for two spin cutoff models with a coincidence time window $\Delta t =$ 3 ns and without detection energy threshold. The energy binning is set to 750 keV.

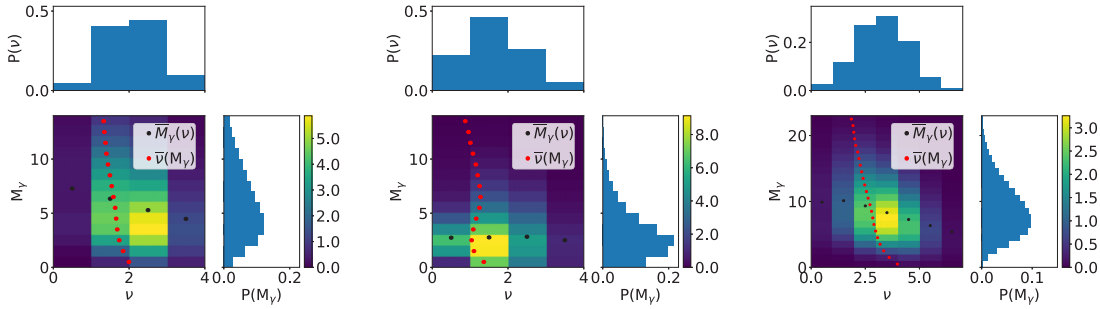

(a) *Light FF,* E_n=0.8 *MeV.* (b) *Heavy FF,* E_n=0.8 *MeV.* (c) *Both FF,* E_n=0.8 *MeV.*

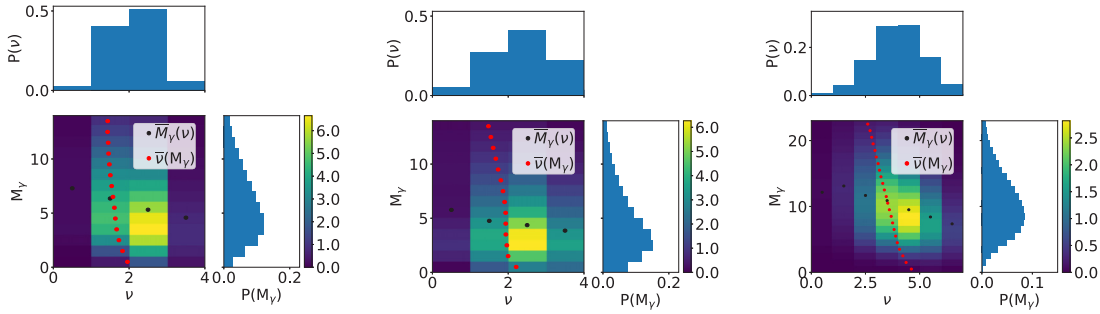

(d) *Light FF,* E_n=5.5 *MeV.* (e) *Heavy FF,* E_n=5.5 *MeV.* (f) *Both FF,* E_n=5.5 *MeV.*

FIG. 12. Constant spin cutoff model: neutron-γ multiplicity correlation matrices (center) with the neutron (top) and γ (left) multiplicity probability distributions, for ^{237}Np(n, f) reactions at 0.8 and 5.5 MeV energies, with a coincidence time window $\Delta t = 3$ ns and without detection energy threshold. The z axis (colored axis) is in 10^{-2} units.

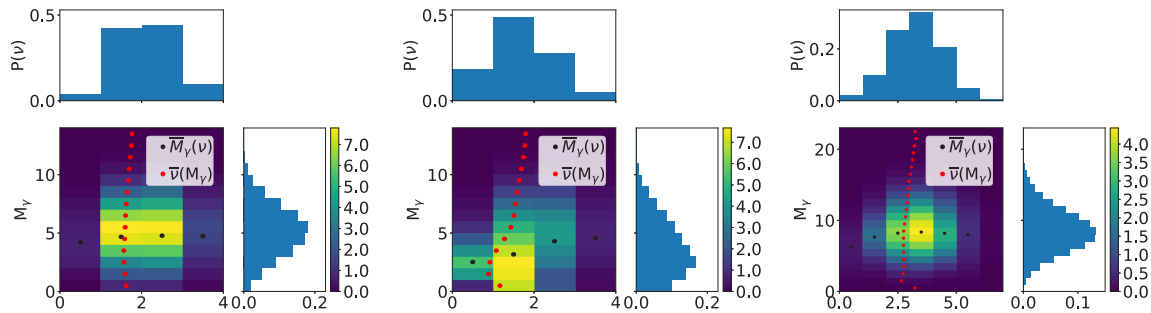

(a) *Light FF,* E_n=0.8 *MeV.* (b) *Heavy FF,* E_n=0.8 *MeV.* (c) *Both FF,* E_n=0.8 *MeV.*

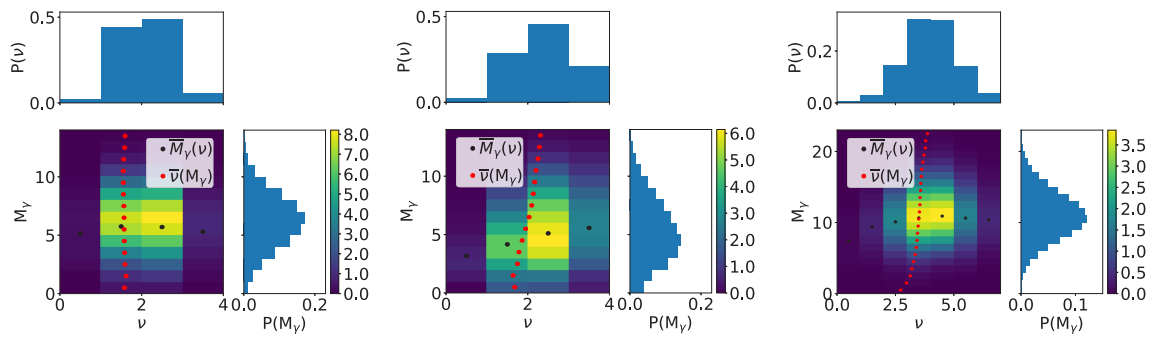

(d) *Light FF,* E_n=5.5 *MeV.* (e) *Heavy FF,* E_n=5.5 *MeV.* (f) *Both FF,* E_n=5.5 *MeV.*

FIG. 13. Energy dependent spin cutoff model: neutron-γ multiplicity correlation matrix (center) with the neutron (top) and γ (left) multiplicity probability distributions, for ^{237}Np(n, f) reactions at 0.8 and 5.5 MeV energies, with a coincidence time window $\Delta t = 3$ ns and without detection energy threshold. The z axis (colored axis) is in 10^{-2} units.

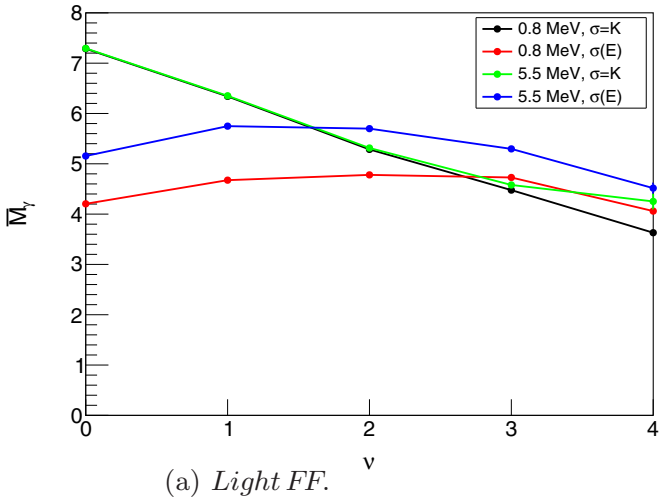

(a) *Light FF.*

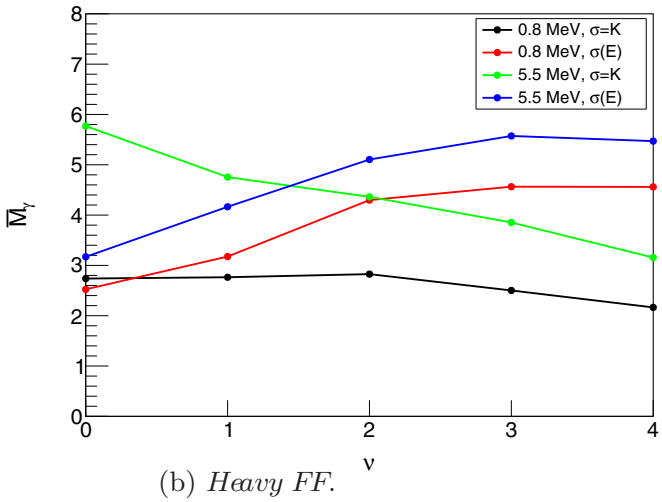

(b) *Heavy FF.*

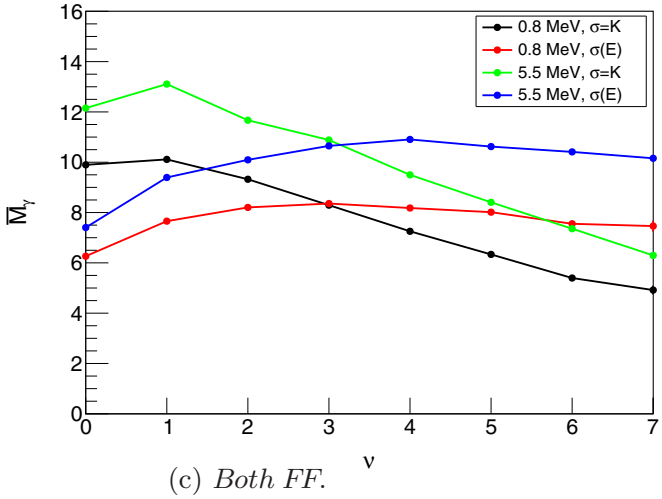

(c) *Both FF.*

FIG. 14. Evolution of the average γ multiplicity as a function of the neutron multiplicity for the ^{237}Np(n, f) reactions at 0.8 and 5.5 MeV neutron energies, with a coincidence time window $\Delta t =$ 3 ns and without detection energy threshold, and for two spin cutoff models.

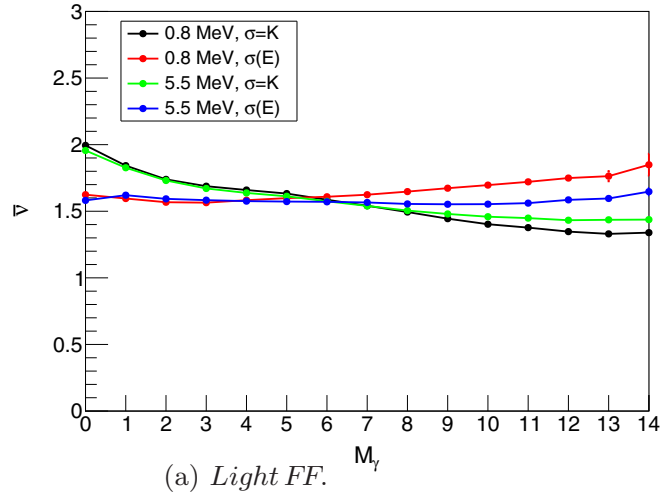

(a) *Light FF.*

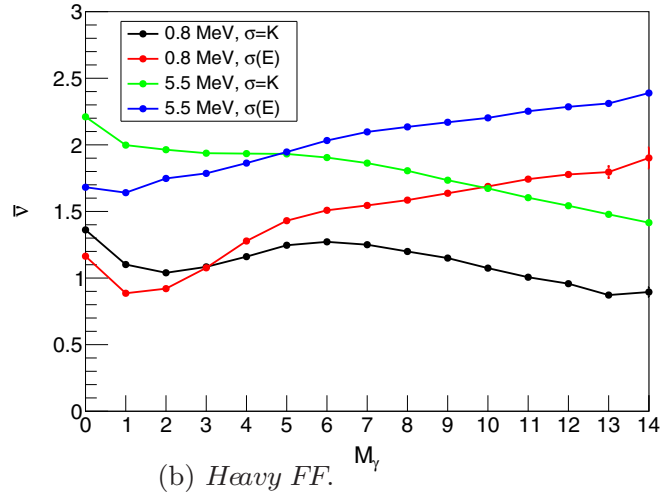

(b) *Heavy FF.*

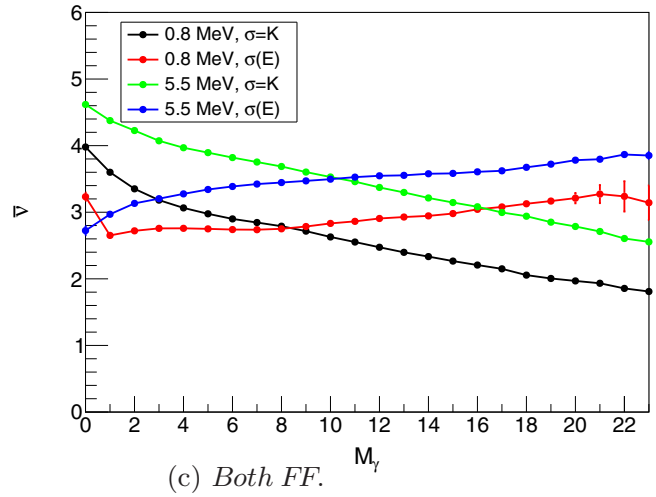

(c) *Both FF.*

FIG. 15. Evolution of the average neutron multiplicity as a function of the γ multiplicity for the ^{237}Np(n, f) reactions at 0.8 and 5.5 MeV neutron energies, with a coincidence time window $\Delta t =$ 3 ns and without detection energy threshold, and for two spin cutoff models.

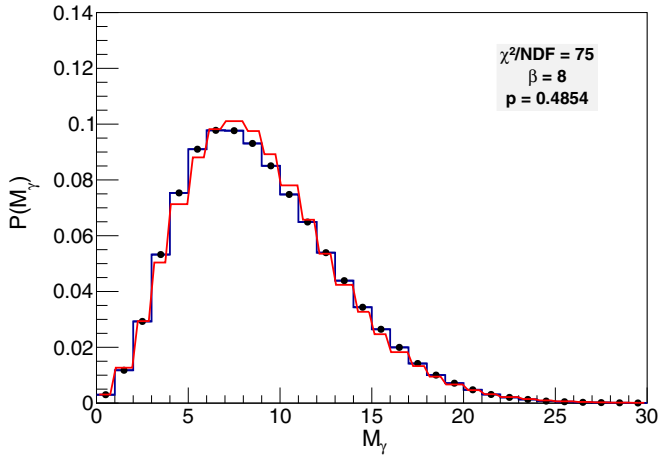

(a) E_n=0.8 *MeV, Constant spin cut–off model.*

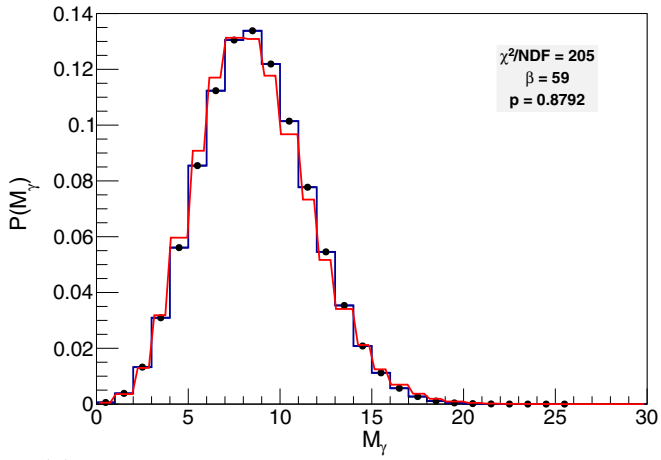

(b) E_n=0.8 *MeV, Energy dependent spin cut–off model.*

FIG. 16. Total prompt γ multiplicity distributions for the ^{237}Np(n, f) reactions at 0.8 MeV neutron energy, with a coincidence time window $\Delta t = 3$ ns and without detection energy threshold, for two spin cutoff models. The distributions are fitted with a negative binomial distribution (red line). β and p are related by $\overline{M}_\gamma = (1 - p)\beta/p$.

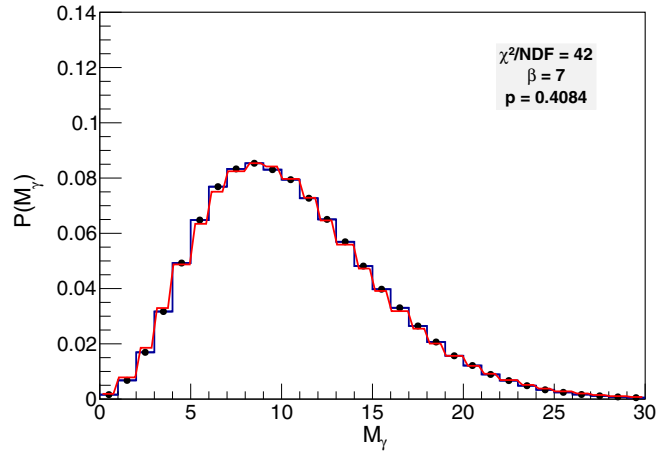

(a) E_n=5.5 *MeV, Constant spin cut–off model.*

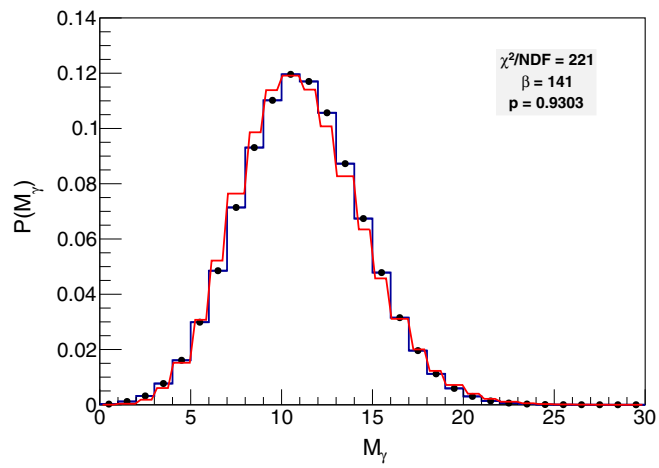

(b) E_n=5.5 *MeV, Energy dependent spin cut–off model.*

FIG. 17. Total prompt γ multiplicity distributions for the ^{237}Np(n, f) reactions at 5.5 MeV neutron energy, with a coincidence time window $\Delta t = 3$ ns and without detection energy threshold, for two spin cutoff models. The distributions are fitted with a negative binomial distribution (red line). β and p are related by $\overline{M}_\gamma = (1 - p)\beta/p$.

relationship between the fragment initial excitation energy and its initial total angular momentum is then investigated here by studying the evolution of $\overline{\nu}$ and $\overline{M}_\gamma$ as a function of TKE (which is an observable anticorrelated to TXE) and in looking at ν-M_γ correlation matrices built on an event-by-event basis.

The impact of TKE and E_n variations on $\overline{\nu}$ and $\overline{M}_\gamma$ are presented in Fig. 11. This figure shows that $\overline{M}_\gamma$(TKE) have a complex shapes and cannot be described with linear regressions as for $\overline{\nu}$(TKE). These $\overline{M}_\gamma$(TKE) curves are now discussed from right to left. For TKE > 200 MeV ($\overline{\nu} = 0$), $\overline{M}_\gamma$ increases with TXE. When the fragment initial excitation energy increases its initial state shifts from the nucleus level scheme discrete part to its continuum part, *i.e.* in average from $E2$ to $E1$ γ emission leading to a higher $\overline{M}_\gamma$. For 185 < TKE < 200 MeV ($0 < \overline{\nu} \leqslant 1$), $\overline{M}_\gamma$ still increases. At E_n = 0.8 MeV, $\overline{M}_\gamma$ has a peak around TKE = 192.5 MeV related to a lower increase of $\overline{\nu}$(TKE). This behavior, not present at $E_n = 5.5$ MeV, is then related to the input data. Finally for 140 < TKE < 185 MeV ($\overline{\nu} > 2$), $\overline{M}_\gamma$(TKE) shape is driven by the spin cutoff model. With the *constant* model $\overline{M}_\gamma$ linearly increases by 0.5 γ's, while with the *energy dependent* model $\overline{M}_\gamma$ increases as a square root function of TXE [Eq. (1)] and varies by +1.5 γ's. Wang's results obtained for ^{252}Cf(sf) (Fig. 8 in Ref. [7]) are not detailed enough to test the model validity with the help of the $\overline{M}_\gamma$(TKE) shape. Experiments having access to $\overline{M}_\gamma$(TKE) as a function of E_n could allow one to infer about the model validity by looking at $\overline{M}_\gamma$ variations for TKE between 140 and 185 MeV.

The relationship between the fragment initial excitation energy and initial total angular momentum can also be investigated on an event-by-event basis with ν-M_γ correlation matrices. From the *constant* and *energy dependent* matrices, respectively presented in Figs. 12 and 13, the average values $\overline{M}_\gamma(\nu)$ and $\overline{\nu}(M_\gamma)$ for the light, heavy, and both fragments are computed and shown in Figs. 14 and 15. $\overline{M}_\gamma(\nu)$ and $\overline{\nu}(M_\gamma)$

show that ν-M_γ correlations are linear and negative with the *constant* model, while they are positive with a more complex shape with the *energy dependent* model. The negative trends predicted by the *constant* model were expected because the spin cutoff parameter is set once for all at the beginning of the energy sharing process (Sec. II B). With the *energy dependent* model $\overline{M}_\gamma(\nu)$ increases and then decreases slowly (it is almost a constant), showing that the neutron emission decreases the total angular momentum. Here, whatever the fragment mass group is, $\overline{M}_\gamma(\nu)$ at $E_n = 5.5$ MeV is roughly $\overline{M}_\gamma(\nu)$ at $E_n = 0.8$ MeV shifted by a given value. Besides, $\overline{\nu}(M_\gamma)$ (Fig. 15) unsurprisingly shows that $\overline{\nu}$ increases with M_γ. At the moment the available experimental ^{252}Cf(sf) data [none exists for ^{237}Np(n, f) reactions] does not allow one to infer about the two spin cutoffs' validities. However, it is worth mentionning that the *energy dependent* model predicts trends similar to the ones determined by Wang for the different mass groups (Figs. 5, 6, and 7 in Ref. [7]). As the two spin cutoff models predict distinctive trends for $\overline{M}_\gamma(\nu)$ and $\overline{\nu}(M_\gamma)$, future experiments determining neutron and γ multiplicity correlations as a function of E_n will allow one to unambiguously infer about their validity.

Another way to probe the initial total angular momentum generation process is to look at the $P(M_\gamma)$ distribution, which is correlated to the $P(J|\sigma)$ distribution, presented on the right sides of the matrices in Figs. 12 and 13. At a given E_n, both models predict approximately the same $P(\nu)$ but different $P(M_\gamma)$. The $P(M_\gamma)$ distributions, which are experimentally accessible, have been fitted with Rayleigh and negative binomial (negBin) distributions. The negBin distributions fit better $P(M_\gamma)$ with χ^2/NDF values around 40 (*constant* model) and 220 (*energy dependent* model), as presented in Figs. 16 and 17. For both spin cutoff models, i.e., independently of the $P(J)$ distribution shape, $P(M_\gamma)$ are well fitted by a negBin distribution. These fits are far from perfect but allow one to encapsulate the main $P(M_\gamma)$ shape differences between the models. The fit parameters will allow direct comparisons with experimental data.

To conclude, correlated fission observables have been presented for two spin cutoff models. Since few experimental data are in the literature and none for fast fission reactions, no conclusion can be drawn on their validity. Since the two models predict different correlation trends, experiments that will determine either $\overline{M}_\gamma$(TKE), ν-M_γ correlation matrices, or $P(M_\gamma)$ would be helpful to infer about their validity (Figs. 16 and 17).

IV. CONCLUSIONS AND PERSPECTIVES

This paper has shown that the FIFRELIN fission fragment deexcitation code reproduces the energy dependence of the experimental neutron multiplicity as a function of the mass determined by Müller and Naqvi for the ^{237}Np(n, f) reactions at 0.8 and 5.5 MeV incident neutron energies. The overall neutron multiplicity experimental data as a function of E_n are well reproduced in assigning the fragment initial states with an energy dependent $R_T(A)$ law in considering fission fragments behaving as a Fermi gas. The evolution of $R_T(A)$ when the incident neutron energy increases leads to a large increase of the heavy fragment temperature while the light one does not change a lot. The choice of a constant or an energy dependent spin cutoff model does not have a significant impact on the neutron observables as long as the initial total angular momentum of the heavy fragment increases on average by 4.5 $\hbar$. Overall this study validates the initial state assignment procedure in FIFRELIN for the fast fission energy range, which was already validated for spontaneous and thermal fission energy ranges [15]. Although the two spin cutoff models predict similar neutron observables, their γ predictions are very different. Therefore, to infer about the different models' relevance, i.e., on a weak or a strong relationship between the fragment initial excitation energy and total angular momentum, it has been pointed out that it is necessary to experimentally determine γ multiplicity distributions and γ multiplicity as a function of the primary fragment mass or total kinetic energy and in correlation with the neutron multiplicity.

In the near future more experimental data should be available since new facilities such as Neutrons For Science (NFS) [44] will provide high neutron fluxes in the MeV energy domain. In addition new 2E-2V spectrometers dedicated to fission studies are currently under construction [45–48] and some will be dedicated to study fast fission reactions.

ACKNOWLEDGMENT

This work is partly supported by the "Investments for the future" programs P2IO LabEx (ANR-10-LABX-0038).

[1] R. Müller, A. A. Naqvi, F. Kaeppeler, and Z. Y. Bao, Report No. KFK–3220, Kernforschungszentrum Karlsruhe G.m.b.H., Germany, F.R., 1981.
[2] A. A. Naqvi, F. Käppeler, F. Dickmann, and R. Müller, Phys. Rev. C **34**, 218 (1986).
[3] A. Ruben *et al.*, Z. Phys. A **338**, 67 (1991).
[4] K.-H. Schmidt, B. Jurado, C. Amouroux, and C. Schmitt, Nucl. Data Sheets **131**, 107 (2016).
[5] C. Morariu, A. Tudora, F.-J. Hambsch, S. Oberstedt, and C. Manailescu, J. Phys. G: Nucl. Part. Phys. **39**, 055103 (2012).
[6] H. Nifenecker, C. Signarbieux, M. Ribrag, J. Poitou, and J. Matuszek, Nucl. Phys. A **189**, 285 (1972).
[7] T. Wang *et al.*, Phys. Rev. C **93**, 014606 (2016).
[8] M. J. Marcath *et al.*, Phys. Rev. C **97**, 044622 (2018).
[9] W. John, J. J. Wesolowski, and F. Guy, Phys. Lett. B **30**, 340 (1969).
[10] H. R. Bowman, J. C. D. Milton, S. G. Thompson, and W. J. Swiatecki, Phys. Rev. **129**, 2133 (1963).
[11] P. Talou, T. Kawano, and I. Stetcu, Nucl. Data Sheets **118**, 195 (2014).
[12] P. Glässel, R. Schmid-Fabian, D. Schwalm, D. Habs, and H. U. v. Helmolt, Nucl. Phys. A **502**, 315 (1989).
[13] J. Fréhaut, Report No. INDC(NDS)–220, CEA Centre d'Etudes de Bruyeres-le-Chatel, France, 1989.

[14] O. Litaize and O. Serot, Phys. Rev. C **82**, 054616 (2010).
[15] O. Litaize, O. Serot, and L. Berge, Eur. Phys. J. A **51**, 177 (2015).
[16] D. Regnier, O. Litaize, and O. Serot, Comput. Phys. Commun. **201**, 19 (2016).
[17] L. Thulliez, O. Litaize, and O. Serot, EPJ Web Conf. **111**, 10003 (2016).
[18] O. Litaize, L. Thulliez, O. Serot, A. Chebboubi, and P. Tamagno, EPJ Web Conf. **169**, 00012 (2018).
[19] A. C. Wahl, At. Data Nucl. Data Tables **39**, 1 (1988).
[20] A. C. Wahl, LANL Report No. LA-13928, 2002 (unpublished).
[21] F. Bečvář, Nucl. Instrum. Methods Phys. Res. A **417**, 434 (1998).
[22] A. Gilbert and A. G. W. Cameron, Can. J. Phys. **43**, 1446 (1965).
[23] R. Capote *et al.*, Nucl. Data Sheets **110**, 3107 (2009).
[24] A. J. Koning and J. Delaroche, Nucl. Phys. A **713**, 231 (2003).
[25] J. Kopecky and M. Uhl, Phys. Rev. C **41**, 1941 (1990).
[26] T. Kibédi, T. W. Burrows, M. B. Trzhaskovskaya, P. M. Davidson, and C. W. Nestor, Nucl. Instruments Methods Phys. Res. Sect. A Accel. Spectrometers, Detect. Assoc. Equip. **589**, 202 (2008).
[27] H. A. Bethe, Phys. Rev. **50**, 332 (1936).
[28] A. V. Ignatyuk, G. N. Smirenkin, and A. S. Tishin, Sov. J. Nucl. Phys. **21**, 255 (1975).
[29] S. K. Kataria, V. S. Ramamurthy, and S. S. Kapoor, Phys. Rev. C **18**, 549 (1978).
[30] S. Goriely, Nucl. Phys. A **605**, 28 (1996).
[31] https://www-nds.iaea.org/exfor
[32] L. R. Veeser, Phys. Rev. C **17**, 385 (1978).
[33] Y. A. Khokhlov *et al.*, in *International Conference on Nuclear Data for Science and Technology* Gatlinburg, TN, May 9–13, 1994 (ANS, La Grange Park, IL, 1994), p. 272.
[34] V. V. Malinovskii, V. G. Vorob'eva, B. D. Kuz'minov, V. M. Piksaikin, N. N. Semenova, S. M. Solov'ev, and P. S. Soloshenkov, Sov. At. Energy **54**, 226 (1983).
[35] J. Taieb *et al.*, in *ND 2007, International Conference on Nuclear Data for Science and Technology*, Nice, April 22–27, 2007 (EDP Sciences, Les Ulis, France, 2007), p. 429.
[36] https://www.oecd-nea.org/dbdata/jeff/jeff33/index.html
[37] J. Fréhaut *et al.*, in *Nuclear Data for Science and Technology, Proceedings of the International Conference*, Antwerp, 6–10 September 1982 (Springer, Berlin, 1983), p. 78.
[38] K.-H. Schmidt and B. Jurado, Phys. Rev. Lett. **104**, 212501 (2010).
[39] T. von Egidy and D. Bucurescu, Phys. Rev. C **72**, 044311 (2005).
[40] J. R. Nix and W. J. Swiatecki, Nucl. Phys. **71**, 1 (1965).
[41] V. M. Strutinskii, J. Exp. Theor. Phys. **37**, 613 (1959).
[42] J. O. Rasmussen, W. Nörenberg, and H. J. Mang, Nucl. Phys. A **136**, 465 (1969).
[43] M. Zielinska-Pfabé and K. Dietrich, Phys. Lett. B **49**, 123 (1974).
[44] X. Ledoux *et al.*, Nucl. Data Sheets **119**, 353 (2014).
[45] D. Doré, F. Farget, F.-R. Lecolley, G. Lehaut, T. Materna, J. Pancin, S. Panebianco, and Th. Papaevangelou, Nucl. Data Sheets **119**, 346 (2014).
[46] M. O. Fregeau, S. Oberstedt, Th. Gamboni, W. Geerts, F.-J. Hambsch, and M. Vidali, Nucl. Instruments Methods Phys. Res. Sect. A Accel. Spectrometers, Detect. Assoc. Equip. **817**, 35 (2016).
[47] K. Meierbachtol *et al.*, Nucl. Instrum. Methods Phys. Res. A **788**, 59 (2015).
[48] J. Mattaranz, I. Tsekhanovich, A. G. Smith, J. A. Dare, L. Murray, A. J. Pollitt, T. Soldner, U. Koster, and D. C. Biswas, Phys. Procedia **47**, 76 (2013).